ELSEVIER

Contents lists available at ScienceDirect

Computers in Biology and Medicine

journal homepage: www.elsevier.com/locate/compbiomed



Evaluation of light detector surface area for functional Near Infrared Spectroscopy



Lei Wang ^{a,b,*}, Hasan Ayaz ^{a,b,c,d}, Meltem Izzetoglu ^{a,b}, Banu Onaral ^{a,b}

- ^a School of Biomedical Engineering, Science & Health Systems, Drexel University, Philadelphia, PA, USA
- b Cognitive Neuroengineering and Quantitative Experimental Research (CONQUER) Collaborative, Drexel University, Philadelphia, PA, USA
- ^c Department of Family and Community Health, University of Pennsylvania, Philadelphia, PA, USA
- d The Division of General Pediatrics, Children's Hospital of Philadelphia, Philadelphia, PA, USA

ARTICLE INFO

Keywords: Functional Near Infrared Spectroscopy Detector surface area Differential pathlength factor Monte Carlo simulation Modified Beer-Lambert law

ABSTRACT

Functional Near Infrared Spectroscopy (fNIRS) is an emerging neuroimaging technique that utilizes near infrared light to detect cortical concentration changes of oxy-hemoglobin and deoxy-hemoglobin non-invasively. Using light sources and detectors over the scalp, multi-wavelength light intensities are recorded as time series and converted to concentration changes of hemoglobin via modified Beer-Lambert law. Here, we describe a potential source for systematic error in the calculation of hemoglobin changes and light intensity measurements. Previous system characterization and analysis studies looked into various fNIRS parameters such as type of light source, number and selection of wavelengths, distance between light source and detector. In this study, we have analyzed the contribution of light detector surface area to the overall outcome. Results from Monte Carlo based digital phantoms indicated that selection of detector area is a critical system parameter in minimizing the error in concentration calculations. The findings here can guide the design of future fNIRS sensors.

1. Introduction

Functional Near Infrared Spectroscopy (fNIRS) is a neuroimaging modality which allows investigation of brain functions non-invasively. It is widely used to measure changes in the concentration of oxyhemoglobin and deoxy-hemoglobin in tissue [1,2]. Infrared light propagates through the tissue and eventually part of it is back-scattered to the surface and collected by photon detector. The detected attenuated light encodes information about brain activity as a consequence of absorption and scattering dominated light tissue interaction. A number of light migration models have been developed to study the transmission process, the majority of the proposed modelling approximation fall into two categories of being either analytical or numerical methods [3-11]. Analytical models have the advantage of fast computation, but limits to simple geometries [12-14]. On the other hand, numerical models are capable of modelling complex geometries, but require relatively higher computational cost. One of the major computational methods in numerical algorithm is Monte Carlo simulation.

The Monte Carlo method refers to numerical simulation based on random sampling from appropriate probability distribution [15–18]. Light is considered as a packet of photons propagated in a certain

direction for a fixed step size within the medium. Whether certain random amount of photon should be absorbed or scattered depends on the material's optical property at specific location [7]. Monte Carlo simulations can model how photons travel through different tissue layers, under dynamically and spatially changing conditions for various fNIRS instrumentations, source-detector types and locations, which is more flexible and informative than physical testing. It has several additional merits such as simple implementation, the ability to handle complex geometries and inhomogeneity, as well as the possibility to incorporate time-dependency.

Several photon migration models have been developed to investigate light tissue interaction. Different aspects of system parameters have been explored, such as wavelength selection, source-detector separation, depth of penetration, and effect of layers' thicknesses [19–25]. Among those simulation studies, most have not declared the detector fiber size, clearly. In some studies it was stated that larger detector surface area could increase the amount of collected light, but could also introduce artifacts and be more easily obstructed by hair [26,27]. The idea of fiber brush to overcome this drawback was proposed, to make the fiber optode molded to fit the diameter of any fiber bundle, with single brush fiber radius as 0.125 mm [28]. However, various fiber sizes have been used in

http://dx.doi.org/10.1016/j.compbiomed.2017.07.019

Received 14 April 2017; Received in revised form 20 July 2017; Accepted 28 July 2017

0010-4825/© 2017 Elsevier Ltd. All rights reserved.

^{*} Corresponding author. School of Biomedical Engineering, Science & Health Systems, Drexel University, Philadelphia, PA, USA. E-mail address: lw474@drexel.edu (L. Wang).

several existing NIRS devices, and fiber radius can be ranged from 0.4 mm to 5.5 mm, as listed in Table 1. Thus, detector fiber size could in fact be an important system parameter and should be investigated in the simulation model, to obtain more accurate estimation of the chromophore concentrations.

In this study, our aim is to point out one of the system parameters, light detector surface area, as a potential source of systematic error in calculating concentrations. To do so, we first introduce the definition of differential pathlength factor (DPF), which is the scaling factor that relates source-detector separations to the average pathlength light travels between the light source and detector. We argue that there is a potential source of error to be considered when analyzing raw fNIRS data using modified Beer-Lambert law (MBLL), that is the detector area that could lead to relative differences in DPF as a function of wavelength. We investigated the effect of the detector surface with Monte Carlo simulations on a digital multilayer model. The results of this approach could be used to optimize fNIRS sensors and provide guidance for the design of next generation optical brain imaging systems.

2. Method

In order to set the theoretical framework for analysis, modified Beer-Lambert law as applied to quantifying concentration changes of deoxyhemoglobin and oxy-hemoglobin is briefly reviewed.

2.1. Modified Beer-Lambert law

The Beer-Lambert law (BLL) is a model that describes the loss of light intensity mainly due to absorption as a function of the concentration of a substance in a non-scattering medium, as in equation (1) [58], I_0 is the incident light, $\varepsilon(\lambda)$ is the wavelength dependent specific extinction coefficient of the chromophore, c is the concentration of the chromophore responsible for the absorption and l is path length.

$$I = I_0 * 10^{-\epsilon(\lambda)^* c^* I} \tag{1}$$

Since biological tissue is highly scattering, in order to use the relation defined by BLL, modified Beer-Lambert law (MBLL) [59] has been introduced and is commonly used in the field of near-infrared spectroscopy for the calculation of oxygenation from light intensity values. MBLL incorporates two elements to the BLL: the differential pathlength factor (DPF) that accounts for the increased distance that the light travels due to scattering and absorption effects, from light source to detector, and a factor $G(\lambda)$ accounting for tissue geometry and light attenuation due to scattering [26,60]. Then, the MBLL is expressed as given in equations (2) and (3) where d accounts for the direct distance between light source and detector.

Detector Source- detector Market radius (mm) Separation (mm) Infrascanner, PA, US Infrascanner 1000 & 2000 0.75 40 Yes [29,30] fNIR1100 ≈1.3 25 fNIR devices, MD, US [31.32] Yes fNIR1200 25 ~1.2 Yes [31,33] TechEn, MA, US CW6 0.5-1.510, 30 Yes [34-36] ISS, IL, US Imagent 1.5, 2 30, 35 [37-41] Yes [42,43] NIRx, Berlin, Germany NIRscout 1.25, 1.5 20 - 30Yes Hitachi, Japan ETG-4000 0.8 30 Yes [44] NIR OT 0.5 20 [45] Yes Hamamatsu, Japan NIRO-200 1.5 30 Yes [46] Oxymon Mk III 35 Artinis Medical Systems, Netherlands 2, 2.25 [47,48] Yes Physikalisch-Technische Bundesanstalt, Humboldt University, Berlin, Germany trNIRS 2 30 Nο [49,50] CNRS-Universite de Strasbourg, Strasbourg Cedex, France trNIRS 0.4 ≈29 [51] No 1.5 Dublin City University, National University of Ireland Maynooth, Ireland CW-fNIRS BCI 30-40 No [52,53] University College London, London, UK UCL Optical Topography System 1.5 15.8, 25, 38.1 No [54] Korea University, Seoul, South Korea Wireless NIRS System ≈1.13 ≈32.1 No Pusan National University, Busan, South Korea Wireless NIRS Systems ≈5.47 30 No [56,57]

$$I = I_0 * 10^{-[\varepsilon(\lambda)^* c^* l + G(\lambda)]}$$
 (2)

$$l = DPF(\lambda)^*d \tag{3}$$

The optical density (OD) for a specific input wavelength is the logarithmic ratio of input light intensity and detected light intensity, which is expressed as given in equation (4) based on MBLL [61].

$$OD(\lambda) = -log_{10}\frac{I}{I_0} = \varepsilon(\lambda)^*c^*d^*DPF(\lambda) + G(\lambda)$$
 (4)

Assuming that $G(\lambda)$ is time-invariant, then the change in OD can be found by using measurements obtained at different time instants as expresses in equation (5), the index i denotes all investigated chromophores, commonly the contributions from oxy-hemoglobin and deoxy-hemoglobin [26], $\Delta OD(\lambda)$ is the change in optical density over time relative to a baseline measurement for a given wavelength, $\varepsilon_{\lambda}^{hbr}$ and $\varepsilon_{\lambda}^{hbr}$ are the wavelength dependent extinction coefficients, while Δc^{hbr} and Δc^{hbo} are the concentration changes of deoxy-hemoglobin and oxy-hemoglobin.

$$\Delta OD(\lambda) = \sum_{i} \varepsilon_{i}(\lambda) * \Delta c_{i} * d * DPF(\lambda)$$

$$= (\varepsilon_{j}^{hbr} * \Delta c^{hbr} + \varepsilon_{j}^{hbo} * \Delta c^{hbo}) * d * DPF_{\lambda}$$
(5)

From measurements of optical density at two wavelengths, the concentration changes can be found as given in equation (6).

$$\begin{cases} \Delta OD_{\lambda 1} = \varepsilon_{\lambda 1}^{hbr} * \Delta c^{hbr} * d^*DPF_{\lambda 1} + \varepsilon_{\lambda 1}^{hbo} * \Delta c^{hbo} * d^*DPF_{\lambda 1} \\ \Delta OD_{\lambda 2} = \varepsilon_{\lambda 2}^{hbr} * \Delta c^{hbr} * d^*DPF_{\lambda 2} + \varepsilon_{\lambda 2}^{hbo} * \Delta c^{hbo} * d^*DPF_{\lambda 2} \end{cases}$$

1

$$\begin{cases}
\Delta c^{hbr} = \frac{\frac{\Delta OD_{\lambda 1} * \varepsilon_{\lambda 2}^{hbo}}{d^* DPF_{\lambda 1}} - \frac{\Delta OD_{\lambda 2} * \varepsilon_{\lambda 1}^{hbo}}{d^* DPF_{\lambda 2}} \\
\varepsilon_{\lambda 1}^{hbr} * \varepsilon_{\lambda 2}^{hbo} - \varepsilon_{\lambda 2}^{hbr} * \varepsilon_{\lambda 1}^{hbo}
\end{cases} \\
\Delta c^{hbo} = \frac{\frac{\Delta OD_{\lambda 1} * \varepsilon_{\lambda 2}^{hbr}}{d^* DPF_{\lambda 1}} - \frac{\Delta OD_{\lambda 2} * \varepsilon_{\lambda 1}^{hbr}}{d^* DPF_{\lambda 2}} \\
\varepsilon_{\lambda 1}^{hbo} * \varepsilon_{\lambda 2}^{hbo} - \varepsilon_{\lambda 2}^{hbo} * \varepsilon_{\lambda 1}^{hbr}
\end{cases} (6)$$

Based on equation (6), systematic errors in the choice of the DPF can result in inaccurate estimation of concentration changes, which can lead to cross-talk in the estimated values [60]. In addition, the absolute magnitudes and relative differences in pathlength factors as a function of wavelength is identified as one of the potential sources of error to be considered when analyzing raw fNIRS data using the MBLL [62]. For

some wavelength pairs, it was shown that 20% total difference in DPF could lead to 50% significant magnitude change in computed concentration changes [62].

2.2. Monte Carlo simulation

Human brain is heterogeneous medium, which consists of scalp, skull, cerebrospinal fluid (CSF), grey matter and white matter. A digital phantom with five-layer slab geometry (100 * 100 * 50 mm³) was designed to monitor adult head model. The thickness of each layer was taken as: 5 mm for scalp, 5 mm for skull, 2 mm for CSF, 4 mm for gray matter, and the rest for white matter [63].

Fig. 1 illustrates the five-layer slab human head model and the configuration of source and detectors used in this study. Source-detector separation was set to 30 mm, and detector area fiber radius was selected as 0.2 mm, 0.4 mm, 0.8 mm, 1.2 mm and 1.6 mm. Detector was placed at 4 different directions with the same source-detector separation and 50 random simulations were run for each detector location. In each simulation, 100 million photons were launched from the source. The optical property of each layer used in the simulation are provided in Table 2. Wavelengths in the simulation were selected close to Hitachi ETG-4000 systems, as 690 nm and 830 nm [62,63].

For the simulation package, Mesh-based Monte Carlo Method (MMCM) was adopted in the simulation, which utilizes a tetrahedral mesh to model a complex anatomical structure [8]. The package computed the partial pathlength of each photon within each layer, based on predefined detector location and area, then the mean optical pathlength and differential pathlength factor (DPF) was computed [17]. The simulation was run on hardware supported by Drexel's University Research Computing Facility.

2.3. Concentration calculation

To demonstrate the contribution of detector area on concentration calculation, fNIRS data collected by Hitachi ETG-4000 systems for a previous Motor-Imagery-Based BCI study was re-analyzed [64–66]. Experiment consisted of motor execution and motor imagery task blocks as well as rest periods. During the experiment, subjects performed one of four tasks: right hand, left hand, right foot, or left foot tapping. During motor execution tasks, subjects tap their fingers against their palm for hand tasks, or tap foot and toes on the floor while keeping their heel on the ground for foot tasks. During motor imagery tasks, subjects were instructed to imagine performing these tasks, but refrain from any muscle movement [65]. A total of 22 sessions sample data collected from 5 subjects were used, and DPF values obtained from simulation with

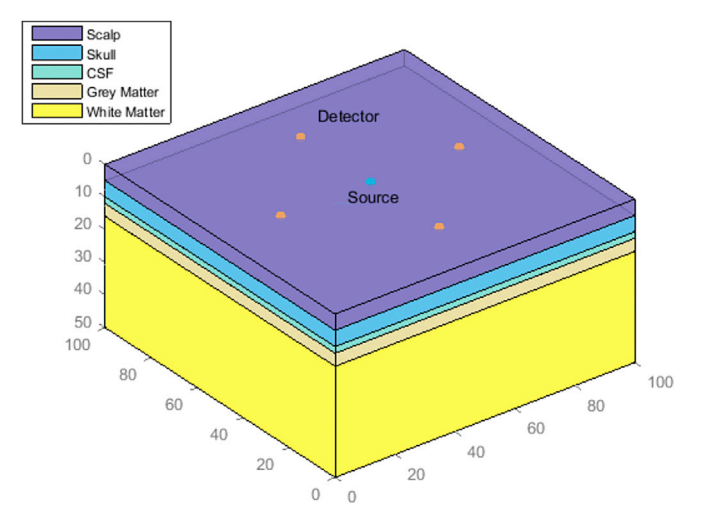


Fig. 1. Geometry of a five-layer slab human head model for Monte Carlo simulations.

Table 2Absorption and scattering coefficients (/mm) from published literature applied in Monte Carlo simulations. Anisotropy was fixed to 0.9 and refractive index to 1.4 in all layers.

		Scalp	Skull	CSF	Gray Matter	White Matter
690 nm	μ _a	0.0162	0.0103	0.0004	0.0182	0.0182
	μ_s	7.87	9.83	0.10	12.29	12.29
830 nm	μ_a	0.0199	0.0141	0.0026	0.0193	0.0193
	μ_{S}	6.47	8.43	0.10	10.88	10.88

different detector active radius were implemented in MBLL process.

For each detector area case in simulation (r=0.2 mm, 0.4 mm, 0.8 mm, 1.2 mm and 1.6 mm), the minimum, maximum and mean value of DPF were obtained through 200 random simulations separately. The minimum versus maximum DPF of two wavelengths were used in MBLL calculation, in equation (6).

3. Results

3.1. Detector area affects DPF stability

Averaged DPF values obtained from simulation for different detector areas (radius: 0.2 mm, 0.4 mm, 0.8 mm, 1.2 mm and 1.6 mm) are shown in Fig. 2 for 690 nm on the left, and 830 nm on the right with sourcedetector separation set to 30 mm. For each detector area size, there were 50 independent simulations per detector location, makes a total of 200 simulations. Each simulation took between 3 and 4 h, with 8 CPU cores. Mean DPF values barely changed as the detector area varied, however, the standard deviations of DPF decreased sharply as detector area increased. There was a statistically significant difference between different detector area as determined by one-way ANOVA $(F(4,15) = 189.399, p < 0.005 \text{ for } \lambda = 690 \text{ nm}, \text{ and } F(4,15) =$ 303.672, p < 0.005 for $\lambda = 830$ nm). A Tukey post hoc test revealed that the standard deviation of DPF values was significantly lower as the detector area increase, there was no statistically significant difference between r = 1.2 mm and r = 1.6 mm groups (p = 0.872 for $\lambda = 690$ nm, and p=0.325 for $\lambda=830$ nm). It was also found that when the detector radius was 0.2 mm, DPF had the largest variation, generating about 25% difference from the mean value ($\lambda = 690$ nm: 25.39%; $\lambda = 830$ nm: 23.90%). While the detector active radius increased to 1.6 mm, DPF values only generated about 3% difference ($\lambda = 690$ nm: 3.05%; $\lambda = 830$ nm: 2.79%). All 200 DPF values for each area size were in Gaussian distribution, except for the case $\lambda = 690$ nm, r = 0.2 mm, as in Fig. 3, upper row shows the distribution of DPFs when wavelength is 690 nm and lower row is for 830 nm, detector area increased from left to right columns.

3.2. DPF variation affects concentration calculation

Using the DPF measurements from the digital head phantom corresponding to different detector area size, oxy-hemoglobin and deoxy-hemoglobin concentration changes were calculated on a pre-recorded data set collected during a Motor-Imagery-Based BCI study as explained before. Resulting hemoglobin concentration changes calculated for different DPF values using single representative data segment (channel 2) are presented in Fig. 4. Upper and lower row of figures represents different chromophores: $\Delta [HbO]$ and $\Delta [HbR]$ respectively. Each column denotes different detector area sizes: 0.4 mm, 0.8 mm and 1.6 mm from left to right. Line type stands for data traces calculated using different DPF pairs: pair 1 is maximum DPF of 690 nm and 830 nm, pair 2 is minimum DPF of 690 nm and 830 nm. In equation (6), the two pairs of DPF values were used to demonstrate the difference in chromophore calculations contributed by detector surface area.

Notable with the curves obtained from detector area with $r=0.4\,\text{mm}$, DPF variation induced a nearly 12% magnitude change in the computed

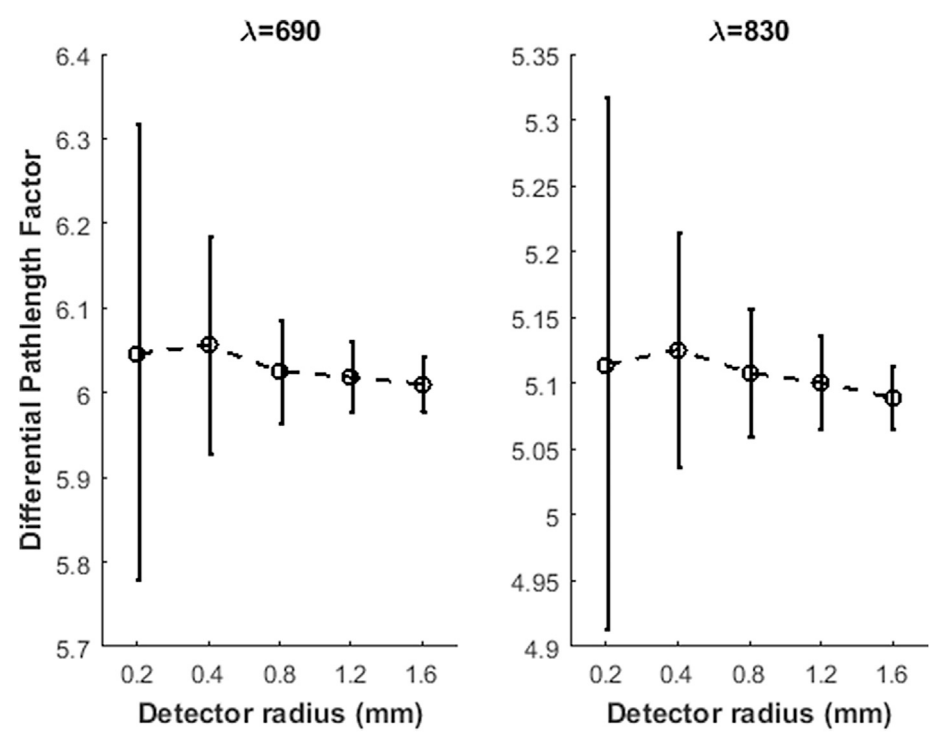


Fig. 2. The effect of light detector area on DPF values (mean \pm std) with different wavelengths measured with Monte Carlo simulation.

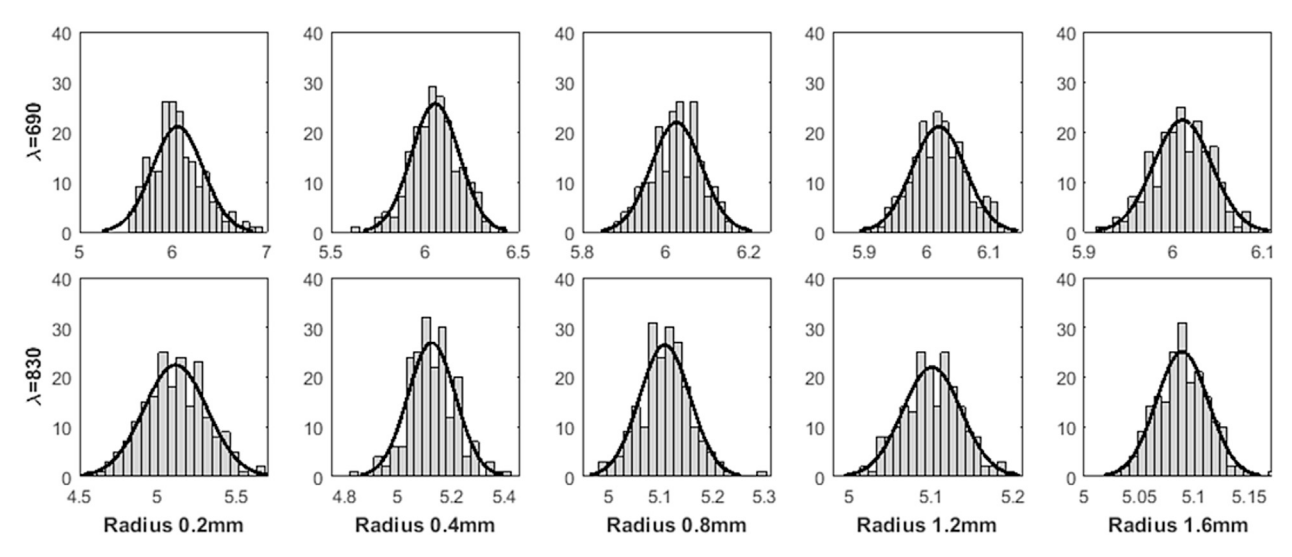


Fig. 3. Distribution of DPF values measured in simulation with different detector radius.

concentrations. The difference was about 6% when r = 0.8 mm, the same size as Hitachi ETG-4000 system (Table 1). When detector area was large as r = 1.6 mm, the difference was only around 3%. A Kruskal-Wallis H test showed that there was a statistically significant difference in mean absolute difference of $\Delta [HbO]$ and $\Delta [HbR]$ between different detector area, $~\chi^4(4)=1104.778,~p=0.000~$ for $~\Delta [HbO],~$ and $~\chi^4(4)=1128.601,~p=0.000$ for $\Delta [HbR].$

The averaged absolute percentage difference of hemoglobin concentration from DPF pairs, across all sample data (5 subjects, 24 channels, 22 sessions in all) is presented in Fig. 5. The difference of oxy-hemoglobin and deoxy-hemoglobin was above 10% when detector area was 0.2 mm and 0.4 mm. The slope of the plot gradually went shallower when detector area was 0.8 mm, still had larger difference than 1.2 mm and 1.6 mm, which only had about 3–5% difference.

$3.3. \ \ Relationship \ of source-detector \ separation \ and \ detector \ area \ with \ DPF$

To further investigate the contribution of detector radius on DPF stability, other source-detector separations were also studied in digital head phantom. Averaged DPF values measured for different detector areas (radius: 0.2 mm, 0.4 mm, 0.8 mm, 1.2 mm and 1.6 mm), and for 690 nm on the top row, and 830 nm on the bottom row where source-detector separation was selected as 10 mm, 15 mm, 20 mm, 25 mm, 30 mm, 35 mm, 40 mm from left to right are presented in Fig. 6. In these calculations, 50 simulations were performed for each condition. The standard deviations of DPF decreased as detector radius increased. When the detector radius was a fixed value, DPF became more unstable with increasing source-detector separations.

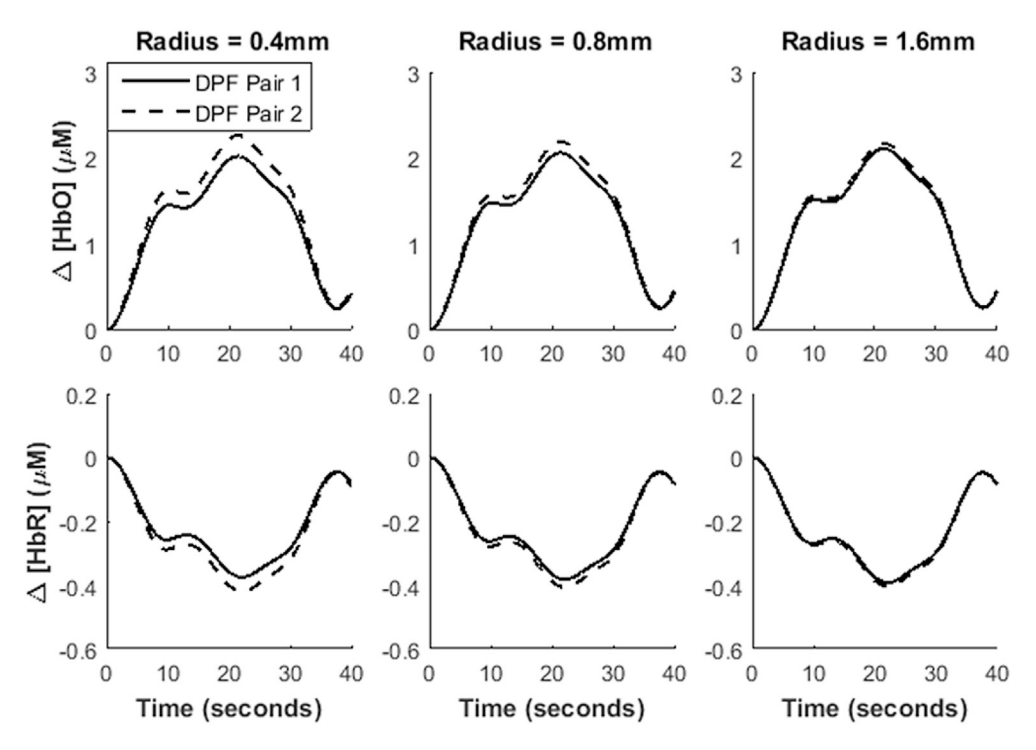


Fig. 4. Comparison of DPF effect on hemoglobin concentration changes with smaller to larger detector area, with detector radiuses 0.4 mm, 0.8 mm and 1.6 mm, are shown left, middle and right, respectively. Hemoglobin concentration changes from the same raw data had the largest deviation due to DPF when detector area was the smallest.

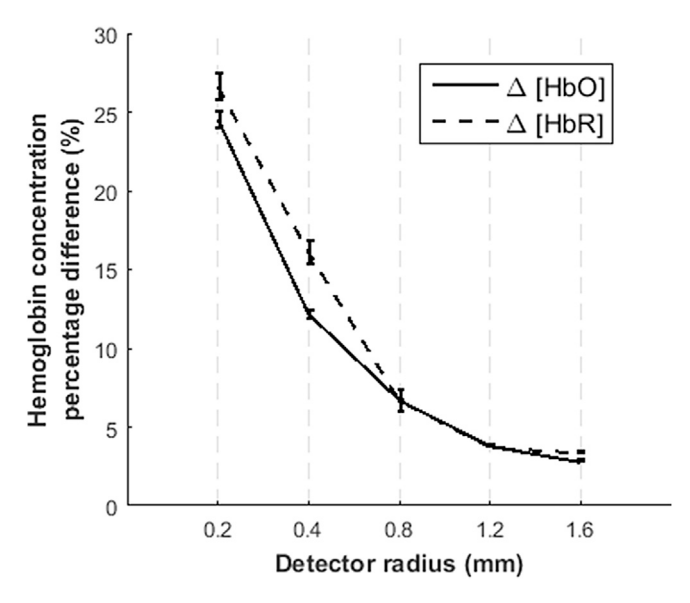


Fig. 5. Averaged percentage change of hemoglobin concentration results due to DPF difference based on detector radius using all demonstration data. Error bars indicate standard error of the mean.

4. Discussion

A variety of systematic errors in recording and processing of NIRS data can lead to unreliable oxy-hemoglobin and deoxy-hemoglobin concentration quantification. In this study, detector surface area is suggested as a potential source of system error in hemoglobin calculation. In order to quantify the error in concentration calculation generated by detector surface area, we performed Monte Carlo simulation on digital phantoms, applied the obtained DPF values from simulations in MBLL on a real measured data set, then computed the contribution of detector area in oxy-hemoglobin and deoxy-hemoglobin concentration calculation.

4.1. DPF stability

Results from simulations indicated that for different detector surfaces areas, when all other aspects are kept the same, the mean DPF for each area size was almost identical. However, detector active radius larger than 1.2 mm acquired more stable DPF value than smaller detector area, such as 0.2 mm. This DPF stability finding was also supported by Monte Carlo simulations with tests on multiple source-detector separations. When source-detector separation was 40 mm, the DPF was noticeably unstable with small detector radius (Fig. 6).

Results in Fig. 6 also suggested that when the detector radius was kept constant, DPF became more unstable as the source-detector separation was increased. With increasing source - detector separation, photons collected by the detector traveled longer pathlength, which could be the contribution to relatively larger standard deviations as compared to smaller separations.

With variations in DPF values, the oxy-hemoglobin and deoxy-hemoglobin concentration calculation using equation (6) would be affected by different amounts. The smaller the variation of DPF values in simulation, the lesser the concentration changes would be impacted.

4.2. Concentration calculation

Results from Fig. 4 implied that more stable DPF values would likely to generate smaller error in hemoglobin calculation. This suggested that relatively larger detector size tend to lead to the calculation of hemoglobin concentration changes more accurately than smaller detector area sizes considering the DPF aspect in MBLL calculations.

The DPF pairs used in the calculation were minimum DPF pair and maximum DPF pair. If the DPF pairs switched, with minimum DPF of 690 nm and maximum DPF of 830 nm as pair one, maximum DPF of 690 nm and minimum DPF of 830 nm as pair two, the difference of DPF used in equation (6) calculation would be around 50%, with $\pm 25\%$ in each wavelength, then much more difference would be generated in concentration changes calculated [62], this could be verified by computation on equation (6). However, with only $\pm 3\%$ difference in each

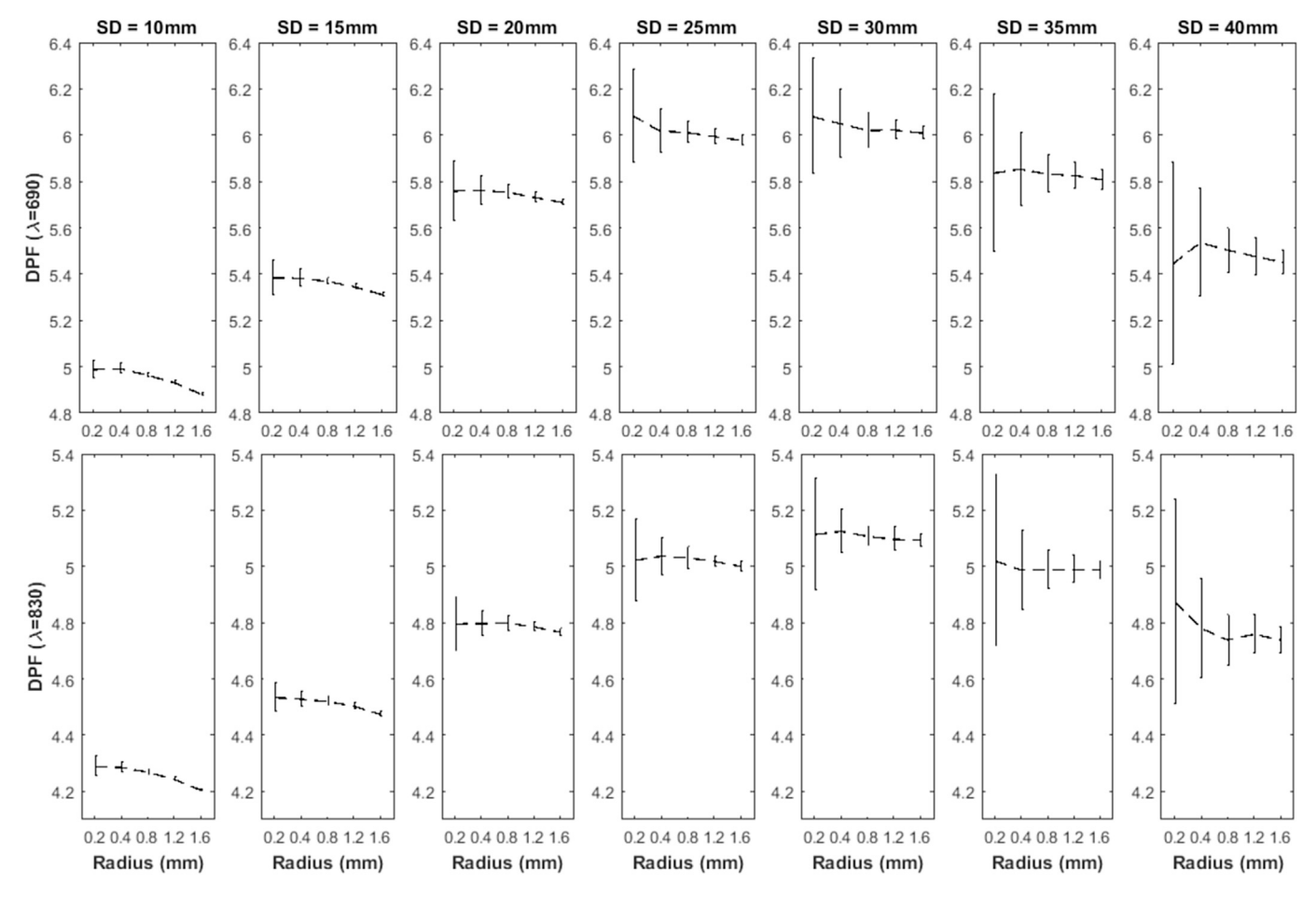


Fig. 6. Comparison of DPF values (mean \pm std) from different detector area varies source-detector (SD = 10 mm-40 mm) separations.

wavelength (r = 1.6 mm), the resulting hemoglobin concentration changes would be affected much less.

Results suggested that too small detector area cannot accurately quantify relative changes in oxy-hemoglobin and deoxy-hemoglobin, especially for large source-detector separations. Thus, detector area r=0.2~mm will be a less optimal choice for oxygenation related measurements, as well as r=0.4~mm (based on Table 1, some NIRS devices have detector fiber bundle as small as about 0.4 mm), cause a relatively small variation in DPF can produce a large error rate in calculated concentration changes. Avoiding this small detector area can therefore help minimize relative error in hemoglobin concentration calculation. Especially when the source-detector separation is relative larger, such as 40 mm, the DPF is much more unstable than smaller separations, introducing the concept of using bundled-optodes which may help minimize the total error rate in concentration calculation [67,68].

In general, from the DPF stability aspect, the relatively larger detector area is preferred. However, if too large detector was selected area, other potential errors could be introduced, such as inaccurate monitoring of focal hemodynamic changes, as discussed in other studies [60]. Given results in Fig. 5, when detector area reached about 0.8 mm, the percentage difference had relatively small changes when the detector area kept increasing, which suggested, radius above 1.2 mm might be an optimal range for detector area selection.

A limitation of this study was the model used in the simulation to acquire the DPFs. We considered human brain as a simple 5-layer slab medium in the simulation, a more complex structure could be introduced, by considering the true head curvature and the spatially varying thickness of extracerebral tissue. Future study would involve more tissue

types and heterogeneous optical properties, the effect of light intensity as well as the light source sizes will also be investigated.

5. Conclusion

In this study, we demonstrated the influence of detector area size on hemoglobin calculation, specifically the DPF stability. Our simulation results showed that as the detector area increases, the DPFs' standard deviation decreases, while the mean DPFs hardly varies, the larger the detector radius, the more stable the DPFs became and hence, with larger detector radius, error rate in hemoglobin calculation was smaller. This overall result highlights the importance of detector area size in fNIRS system design. Since fNIRS recordings are potentially sensitive to several sources of systematic error, some errors can be substantial in causing dramatic differences in the calculation of concentration changes. The choice of appropriate detector area could help minimize such errors.

Acknowledgments

Work reported here was run on hardware supported by Drexel's University Research Computing Facility.

References

- A. Villringer, B. Chance, Non-invasive optical spectroscopy and imaging of human brain function, Trends Neurosci. 20 (10) (1997) 435

 –442.
- [2] G. Strangman, D.A. Boas, J.P. Sutton, Non-invasive neuroimaging using near-infrared light, Biol. psychiatry 52 (7) (2002) 679–693.

- [3] S.R. Arridge, M. Schweiger, Direct calculation of the moments of the distribution of photon time of flight in tissue with a finite-element method, Appl. Opt. 34 (15) (1995) 2683–2687.
- [4] J.C. Schotland, Continuous-wave diffusion imaging, JOSA A 14 (1) (1997) 275–279.
- [5] J. Ripoll, V. Ntziachristos, J.P. Culver, D.N. Pattanayak, A.G. Yodh, M. Nieto-Vesperinas, Recovery of optical parameters in multiple-layered diffusive media: theory and experiments, JOSA A 18 (4) (2001) 821–830.
- [6] S.R. Arridge, Optical tomography in medical imaging, Inverse Probl. 15 (2) (1999) R41.
- [7] L. Wang, S.L. Jacques, L. Zheng, MCML—Monte Carlo modeling of light transport in multi-layered tissues, Comput. methods Programs Biomed. 47 (2) (1995) 131–146.
- [8] Q. Fang, Mesh-based Monte Carlo method using fast ray-tracing in Plücker coordinates, Biomed. Opt. Express 1 (1) (2010) 165–175.
- [9] D. Boas, J. Culver, J. Stott, A. Dunn, Three dimensional Monte Carlo code for photon migration through complex heterogeneous media including the adult human head, Opt. Express 10 (3) (2002) 159–170.
- [10] H. Dehghani, M.E. Eames, P.K. Yalavarthy, S.C. Davis, S. Srinivasan, C.M. Carpenter, B.W. Pogue, K.D. Paulsen, Near infrared optical tomography using NIRFAST: algorithm for numerical model and image reconstruction, Commun. Numer. methods Eng. 25 (6) (2009) 711–732.
- [11] S.T. Flock, M.S. Patterson, B.C. Wilson, D.R. Wyman, Monte Carlo modeling of light propagation in highly scattering tissues. I. Model predictions and comparison with diffusion theory, IEEE Trans. Biomed. Eng. 36 (12) (1989) 1162–1168.
- [12] M.S. Patterson, B. Chance, B.C. Wilson, Time resolved reflectance and transmittance for the noninvasive measurement of tissue optical properties, Appl. Opt. 28 (12) (1989) 2331–2336.
- [13] S.R. Arridge, M. Cope, D. Delpy, The theoretical basis for the determination of optical pathlengths in tissue: temporal and frequency analysis, Phys. Med. Biol. 37 (7) (1992) 1531.
- [14] D. Contini, F. Martelli, G. Zaccanti, Photon migration through a turbid slab described by a model based on diffusion approximation, I. Theory. Appl. Opt. 36 (19) (1997) 4587–4599.
- [15] Y. Hasegawa, Y. Yamada, M. Tamura, Y. Nomura, Monte Carlo simulation of light transmission through living tissues, Appl. Opt. 30 (31) (1991) 4515–4520.
- [16] M. Hiraoka, M. Firbank, M. Essenpreis, M. Cope, S.R. Arridge, P. van der Zee, D.T. Delpy, Monte Carlo simulation of light transport through inhomogeneous tissue, in: OE/LASE'93: Optics, Electro-optics, & Laser Applications in Science& Engineering, International Society for Optics and Photonics, 1993.
- [17] M. Hiraoka, M. Firbank, M. Essenpreis, M. Cope, S. Arridge, P. Van Der Zee, D. Delpy, A Monte Carlo investigation of optical pathlength in inhomogeneous tissue and its application to near-infrared spectroscopy, Phys. Med. Biol. 38 (12) (1993) 1859.
- [18] B. Wilson, G. Adam, A Monte Carlo model for the absorption and flux distributions of light in tissue, Med. Phys. 10 (6) (1983) 824–830.
- [19] Z. Guo, F. Cai, S. He, Optimization for brain activity monitoring with near infrared light in a four-layered model of the human head, Prog. Electromagn. Res. 140 (2013) 277–295.
- [20] T. Takahashi, Y. Takikawa, R. Kawagoe, S. Shibuya, T. Iwano, S. Kitazawa, Influence of skin blood flow on near-infrared spectroscopy signals measured on the forehead during a verbal fluency task, Neuroimage 57 (3) (2011) 991–1002.
- [21] K. Uludağ, J. Steinbrink, A. Villringer, H. Obrig, Separability and cross talk: optimizing dual wavelength combinations for near-infrared spectroscopy of the adult head, Neuroimage 22 (2) (2004) 583–589.
- [22] E. Okada, D.T. Delpy, Near-infrared light propagation in an adult head model, I. Model. low-level Scatt. Cerebrospinal fluid layer. Appl. Opt. 42 (16) (2003) 2906–2914.
- [23] G.E. Strangman, Z. Li, Q. Zhang, Depth sensitivity and source-detector separations for near infrared spectroscopy based on the colin27 brain template, PLos One 8 (8) (2013), e66319.
- [24] C. Mansouri, J.-P. L'Huillier, N.H. Kashou, A. Humeau, Depth sensitivity analysis of functional near-infrared spectroscopy measurement using three-dimensional Monte Carlo modelling-based magnetic resonance imaging, Lasers Med. Sci. 25 (3) (2010) 431–438
- [25] G.E. Strangman, Q. Zhang, Z. Li, Scalp and skull influence on near infrared photon propagation in the Colin27 brain template, Neuroimage 85 (2014) 136–149.
- [26] F. Scholkmann, S. Kleiser, A.J. Metz, R. Zimmermann, J.M. Pavia, U. Wolf, M. Wolf, A review on continuous wave functional near-infrared spectroscopy and imaging instrumentation and methodology, Neuroimage 85 (2014) 6–27.
- [27] A. Torricelli, D. Contini, A. Pifferi, M. Caffini, R. Re, L. Zucchelli, L. Spinelli, Time domain functional NIRS imaging for human brain mapping, Neuroimage 85 (2014) 28–50
- [28] C. Wildey, D.L. MacFarlane, B. Khan, F. Tian, H. Liu, G. Alexandrakis, Improved fNIRS using a novel brush optrode, in: Frontiers in Optics, Optical Society of America, 2010.
- [29] H. Ayaz, B.B. Dor, D. Solt, B. Onaral, Infrascanner: cost effective, mobile medical imaging system for detecting hemotomas, J. Med. Devices 5 (2) (2011) 027540.
- [30] J. Leon-Carrion, J.M. Dominguez-Roldan, U. Leon-Dominguez, F. Murillo-Cabezas, The Infrascanner, a handheld device for screening in situ for the presence of brain haematomas, Brain Inj. 24 (10) (2010) 1193–1201.
- [31] H. Ayaz, B. Onaral, K. Izzetoglu, P.A. Shewokis, R. McKendrick, R. Parasuraman, Continuous monitoring of brain dynamics with functional near infrared spectroscopy as a tool for neuroergonomic research: empirical examples and a technological development, Front. Hum. Neurosci. (2013) 7.

- [32] M. Izzetoglu, K. Izzetoglu, S. Bunce, H. Ayaz, A. Devaraj, B. Onaral, K. Pourrezaei, Functional near-infrared neuroimaging, Neural Syst. Rehabilitation Eng. 13 (2) (2005) 153–159. IEEE Transactions on.
- [33] H. Ayaz, P.A. Shewokis, A. Curtin, M. Izzetoglu, K. Izzetoglu, B. Onaral, Using MazeSuite and functional near infrared spectroscopy to study learning in spatial navigation, JoVE J. Vis. Exp. (56) (2011) e3443.
- [34] L. Gagnon, R.J. Cooper, M.A. Yücel, K.L. Perdue, D.N. Greve, D.A. Boas, Short separation channel location impacts the performance of short channel regression in NIRS, Neuroimage 59 (3) (2012) 2518–2528.
- [35] B.D. Kussman, C.M. Aasted, M.A. Yücel, S.C. Steele, M.E. Alexander, D.A. Boas, D. Borsook, L. Becerra, Capturing pain in the cortex during general anesthesia: near infrared spectroscopy measures in patients undergoing catheter ablation of arrhythmias, PLos One (7) (2016) 11, e0158975.
- [36] P.-Y. Lin, L. Cornelissen, K. Hagan, J. Sutin, Y. Sheldon, K. Chen, E. Grant, C. Berde, M.A. Franceschini, Simultaneous cerebral hemodynamics and blood flow measurements to quantify cerebral metabolism in infants by near-infrared spectroscopy, in: Biomedical Optics, Optical Society of America, 2014.
- [37] Y. Tong, Functional Study of the Brain and Peripheral Nerves Using Near-infrared Spectroscopy, ProQuest, 2008.
- [38] B. Seraglia, L. Gamberini, K. Priftis, P. Scatturin, M. Martinelli, S. Cutini, An exploratory fNIRS study with immersive virtual reality: a new method for technical implementation, Front. Hum. Neurosci. 5 (2011) 176.
- [39] S. Cutini, P. Scatturin, E. Menon, P.S. Bisiacchi, L. Gamberini, M. Zorzi, R. Dell'Acqua, Selective activation of the superior frontal gyrus in task-switching: an event-related fNIRS study, Neuroimage 42 (2) (2008) 945–955.
- [40] S. Cutini, F. Scarpa, P. Scatturin, R. Dell'Acqua, M. Zorzi, Number-space interactions in the human parietal cortex: enlightening the SNARC effect with functional near-infrared spectroscopy, Cereb. Cortex (2012) bhs321.
- [41] A. Zafar, K.-S. Hong, Detection and classification of three-class initial dips from prefrontal cortex, Biomed. Opt. express 8 (1) (2017) 367–383.
- [42] A.D. Zaidi, M.H. Munk, A. Schmidt, C. Risueno-Segovia, R. Bernard, E. Fetz, N. Logothetis, N. Birbaumer, R. Sitaram, Simultaneous epidural functional nearinfrared spectroscopy and cortical electrophysiology as a tool for studying local neurovascular coupling in primates, Neuroimage 120 (2015) 394–399.
- [43] J. Mehnert, Evaluation and Optimization of Recent Analytical Approaches for In-Vivo Measurements with Near-Infrared Spectroscopy, Citeseer, 2012.
- [44] S. Cutini, S.B. Moroa, S. Biscontib, Functional near infrared optical imaging in cognitive neuroscience: an introductory, J. Near Infrared Spectrosc. 20 (1) (2012) 75–92.
- [45] G. Taga, K. Asakawa, A. Maki, Y. Konishi, H. Koizumi, Brain imaging in awake infants by near-infrared optical topography, Proc. Nat. Aca. Sci. 100 (19) (2003) 10722–10727.
- [46] T. Limongi, G. Di Sante, M. Ferrari, V. Quaresima, Detecting mental calculation related frontal cortex oxygenation changes for brain computer interface using multichannel functional near infrared topography, Int. J. Bioelectromagn. 11 (2) (2009) 86-90
- [47] W.N. Colier, V. Quaresima, R. Wenzel, M.C. van der Sluijs, B. Oeseburg, M. Ferrari, A. Villringer, Cortical blood oxygenation changes in the left and right occipital area induced by selective visual stimuli in humans, in: Oxygen Transport to Tissue XXI, Springer, 1999, pp. 35–41.
- [48] S. Basso Moro, S. Cutini, M.L. Ursini, M. Ferrari, V. Quaresima, Prefrontal cortex activation during story encoding/retrieval: a multi-channel functional near-infrared spectroscopy study, Fron. Hum. Neuroscl. 7 (2013) 925.
- [49] T. Sander, A. Liebert, B. Mackert, H. Wabnitz, S. Leistner, G. Curio, M. Burghoff, R. Macdonald, L. Trahms, DC-magnetoencephalography and time-resolved nearinfrared spectroscopy combined to study neuronal and vascular brain responses, Physiol. Meas. 28 (6) (2007) 651.
- [50] A. Liebert, H. Wabnitz, J. Steinbrink, H. Obrig, M. Möller, R. Macdonald, A. Villringer, H. Rinneberg, Time-resolved multidistance near-infrared spectroscopy of the adult head: intracerebral and extracerebral absorption changes from moments of distribution of times of flight of photons, Appl. Opt. 43 (15) (2004) 3037–3047.
- [51] M. Amouroux, W. Uhring, T. Pebayle, P. Poulet, L. Marlier, A safe, low-cost and portable instrumentation for bedside time-resolved picosecond near infrared spectroscopy, in: European Conference on Biomedical Optics, Optical Society of America, 2009.
- [52] S.M. Coyle, T.E. Ward, C.M. Markham, Brain-computer interface using a simplified functional near-infrared spectroscopy system, J. Neural Eng. 4 (3) (2007) 219.
- [53] S. Coyle, T. Ward, C. Markham, G. McDarby, On the suitability of near-infrared (NIR) systems for next-generation brain-computer interfaces, Physiol. Meas. 25 (4) (2004) 815.
- [54] N. Everdell, A. Gibson, I. Tullis, T. Vaithianathan, J. Hebden, D. Delpy, A frequency multiplexed near-infrared topography system for imaging functional activation in the brain, Rev. Sci. Instrum. 76 (9) (2005) 093705.
- [55] C.-K. Kim, S. Lee, D. Koh, B.-M. Kim, Development of wireless NIRS system with dynamic removal of motion artifacts, Biomed. Eng. Lett. 1 (4) (2011) 254–259.
- [56] M.R. Bhutta, K.-S. Hong, B.-M. Kim, M.J. Hong, Y.-H. Kim, S.-H. Lee, Note: three wavelengths near-infrared spectroscopy system for compensating the light absorbance by water, Rev. Sci. Instrum. 85 (2) (2014) 026111.
- [57] M.R. Bhutta, M.J. Hong, Y.-H. Kim, K.-S. Hong, Single-trial lie detection using a combined fNIRS-polygraph system, Front. Psychol. 6 (2015) 709.
- [58] I.-Y. Son, B. Yazici, Near infrared imaging and spectroscopy for brain activity monitoring, in: Advances in Sensing with Security Applications, Springer, 2006, pp. 341–372.

- [59] D.T. Delpy, M. Cope, P. van der Zee, S. Arridge, S. Wray, J. Wyatt, Estimation of optical pathlength through tissue from direct time of flight measurement, Phys. Med. Biol. 33 (12) (1988) 1433.
- [60] D.A. Boas, T. Gaudette, G. Strangman, X. Cheng, J.J. Marota, J.B. Mandeville, The accuracy of near infrared spectroscopy and imaging during focal changes in cerebral hemodynamics, Neuroimage 13 (1) (2001) 76–90.
- [61] H. Ayaz, P.A. Shewokis, S. Bunce, K. Izzetoglu, B. Willems, B. Onaral, Optical brain monitoring for operator training and mental workload assessment, Neuroimage 59 (1) (2012) 36–47.
- [62] G. Strangman, M.A. Franceschini, D.A. Boas, Factors affecting the accuracy of near-infrared spectroscopy concentration calculations for focal changes in oxygenation parameters, Neuroimage 18 (4) (2003) 865–879.
- [63] C. Bonnéry, P.-O. Leclerc, M. Desjardins, R. Hoge, L. Bherer, P. Pouliot, F. Lesage, Changes in diffusion path length with old age in diffuse optical tomography, J. Biomed. Opt. 17 (5) (2012) 0560021–0560028.
- [64] A.M. Batula, J. Mark, Y.E. Kim, H. Ayaz, Developing an optical brain-computer interface for humanoid robot control, in: International Conference on Augmented Cognition, Springer, 2016.
- [65] A.M. Batula, H. Ayaz, Y.E. Kim, Evaluating a four-class motor-imagery-based optical brain-computer interface, in: Engineering in Medicine and Biology Society (EMBC), 2014 36th Annual International Conference of the IEEE, IEEE, 2014.
- [66] A.M. Batula, J.A. Mark, Y.E. Kim, H. Ayaz, Comparison of brain activation during motor imagery and motor movement using fNIRS, Comput. Intell. Neurosci. (2017) 2017
- [67] H.-D. Nguyen, K.-S. Hong, Y.-I. Shin, Bundled-optode method in functional nearinfrared spectroscopy, PLos One (10) (2016) 11, e0165146.
- [68] H.-D. Nguyen, K.-S. Hong, Bundled-optode implementation for 3D imaging in functional near-infrared spectroscopy, Biomed. Opt. Express 7 (9) (2016) 3491–3507.